Journal of Materials Science: Materials in Electronics (2020) 31:4650–4661
https://doi.org/10.1007/s10854-020-03017-2

The critical role of Tween 80 as a 'green' template on the physical properties and photocatalytic performance of TiO_2 nanoparticles for Rhodamine B photodegradation

M. A. Hamza[1] · Z. M. Abou-Gamra[1] · M. A. Ahmed[1] · H. A. A. Medien[1]

Received: 3 December 2019 / Accepted: 29 January 2020 / Published online: 11 February 2020

Abstract

A popular non-toxic surfactant, Tween 80 (T80), is widely used in foods, cosmetics, and pharmaceuticals. This eco-friendly surfactant should be promising to be utilized as a non-ionic template in the preparation of TiO_2 nanoparticles. Moreover, few studies deal with Tween 80 as a template in the synthesis of various nanoparticles. Different concentrations of T80/isopropanol solutions (0–50%) were used in a modified template-assisted sol–gel route, where the synthesized xerogels were denoted by x%T80-TiO_2. Different techniques such as DRS, XRD, SEM, HR-TEM, and N_2 adsorption–desorption isotherms were utilized to characterize the as-prepared x%T80-TiO_2 catalysts. The obtained results showed that the whole physical properties, such as crystalline parameters, optical properties, micromorphology, nanomorphology, and surface parameters, were affected by the concentration of T80 (T80%). In addition, T80% significantly changed the photoactivity of the synthesized samples toward the photodegradation of Rhodamine B (RB) as a pollutant model. 5%T80-TiO_2 nanoparticles were the most reactive catalyst referring to its unique rod structure and existence of a small content of Rutile phase. Finally, tetra (4-carboxyphenyl) porphyrin (TCPP) was anchored on TiO_2 nanorods to be used as a visible antenna to enhance its photocatalytic activity toward the visible light irradiation. Briefly, TCPP-sensitized T80-TiO_2 nanoparticles showed an enhanced performance toward the degradation of RB under various light sources.

1 Introduction

Our world suffers extremely from a severe crisis which is water pollution because of the exceptionally increasing demand of various industries. Textile dyes could be considered as one of the major water pollutants due to the discharge of large quantities of these toxic and carcinogenic organic compounds in the environment; the released amounts are estimated to exceed 100,000 t annually [1, 2]. Green, efficient, and advanced economic water treatment technologies are a crucial point where nanoscience could make a difference in the paradigm shift from the traditional treatment methods to the effective advanced oxidation processes (AOPs). Semiconductor-assisted photocatalysis became one of the most effective AOPs, which considered as a potential solution for encountering pollutant degradation and energy conversion/storage [3, 4]. This process was intensively studied as an economic 'green' method for wastewater treatment operated at only mild temperature/pressure conditions and achieved almost complete degradation with no waste-solids disposal problem [2, 5]. Owing to the high reactivity, large surface area, and super-advantageous properties of nanoparticles with respect to bulk ones, they are utilized in various vital photocatalytic applications such as water treatment, water splitting, and solar cells [4, 6]. In the latest decades, great concern was focused on the development of novel synthesis routes to fabricate distinct nanostructures such as nanospheres, nanorods, and nanotubes. Several methods are employed for this purpose, but the most popular one

Electronic supplementary material The online version of this article (https://doi.org/10.1007/s10854-020-03017-2) contains supplementary material, which is available to authorized users.

✉ M. A. Ahmed
abdelhay71@hotmail.com

M. A. Hamza
mahmoud_adel@sci.asu.edu.eg

Z. M. Abou-Gamra
zanibabougamra@yahoo.com

H. A. A. Medien
hmadian@hotmail.com

[1] Chemistry department, Faculty of Science, Ain-Shams University, Abbassia, Cairo, Egypt

is template-assisted sol–gel, which is characterized by high control and tailoring of both the shape and size of nanoparticles besides its simplicity and low cost. Due to their amphiphilic properties, surfactants could act as templates due to their various micelle structures in solutions, such as cubic, spherical, cylindrical, hexagonal, and lamellar shapes. Thus, the features of surfactants as self-assembled templates is essential to fabricate and tune the pore structure of inorganic materials [7–9].

Titanium oxide (TiO_2) nanoparticles could be the most commonly used photocatalysts because of their non-toxicity, low cost, availability, long durability, chemical stability, photo-stability, and perfect photocatalytic behavior. However, TiO_2 nanoparticles have two main drawbacks: the former is the fast *e–h* recombination rate that reduces their photoactivity, and the latter is the wide bandgap energy (3.2 eV for pure Anatase) leading to exclusive of their photocatalytic performance only under UV irradiation which resembles only 2–3% of solar-light spectrum [10–12]. Different methods were utilized to recover these drawbacks, such as metal doping [13, 14], non-metal doping [15–18], co-doping [19–22], and dye sensitization using phthalocyanine [23], curcumin [24], porphyrins, and metal-porphyrins [25–34]. Porphyrins are intensively colored materials characterized by their strong absorption in the whole visible range [35–37]. Kathiravan and Renganathan [30] studied the influence of the anchoring group of porphyrin on the photosensitization of Titanium dioxide nanoparticles by various porphyrins, among which TCPP was the most effective photosensitizer. In our previous work [38], TCPP and template-free TiO_2 nanoparticles were prepared, and different TCPP loadings were anchored on the surface template-free TiO_2 to determine its optimum loading. TCPP was found to have a brilliant role in improving the entire optical characteristics of TiO_2 by reducing the *e–h* recombination rate, reducing the bandgap energy, and establishment of a perfect antenna to overcome its inefficiency in visible light region.

Polyoxyethylene (20) sorbitan monooleate (Polysorbate 80), commercially recognized as Tween 80, is a popular non-toxic non-ionic surfactant which is widely used in foods, cosmetics, and pharmaceuticals. However, few studies deal with Tween 80 as a template in the preparation of various nanoparticles [39–41]. Therefore, this work focused on the study of the influence of Tween 80 as a green template in the synthesis of TiO_2 nanoparticles. Herein, we have synthesized TiO_2 nanoparticles using different concentrations of T80/isopropanol solutions (0–50%) were used in a modified template-assisted sol–gel method. Various techniques such as DRS, XRD, SEM, HR-TEM, and N_2 adsorption–desorption isotherms were utilized to characterize the synthesized *x*%T80-TiO_2 photocatalysts and to show the effect of T80% on their physicochemical properties. The mechanism of action of T80 as a template is suggested. The photocatalytic activity of *x*%T80-TiO_2 catalysts was assessed by following the degradation of RB dye under UV-A irradiation. Finally, TCPP was anchored on the surface of the most reactive T80-TiO_2 nanoparticles, and its effect on the photocatalytic activity toward RB photodegradation was evaluated under various light sources and compared with the previously prepared TCPP/Template-free TiO_2 nanoparticles.

2 Experimental

2.1 Materials

Tween 80 (T80, Riedel-de Häin), titanium tetra-isopropoxide 97% (TTIP, Sigma-Aldrich), and Rhodamine B (RB, Merck) were purchased. HPLC grades of acetonitrile, methanol, and water were obtained from Fisher Scientific Company. The other chemicals used in this work were used as received without further purification. The dye solutions were prepared with distilled water. The chemical structures of T80, RB, and TCPP are presented in Fig. 1.

2.2 Synthesis of T80-TiO_2 nanoparticles

Simultaneously, five batches of T80-TiO_2 nanoparticles were synthesized through a modified template-assisted sol–gel route (Fig. 2a). Typically, 10 mL of TTIP were mixed with 100 mL of isopropanol. The solutions were stirred using magnetic stirrers at 400 rpm for 1 h. Different concentrations of T80/isopropanol solutions (0, 5, 10, 25 and 50%) were prepared. Then, 5 mL of *x*% T80/isopropanol solutions were added to the five precursor solutions, respectively, and left on stirring for 2 h. Then, the hydrolysis process was performed by the dropwise addition of proper volumes of distilled water to the above solutions where the white colloidal particles increased by the progress of the hydrolysis process until milky-like gels were obtained. After aging for 3 days, the gels were filtered then washed several times using distilled water and isopropanol. Finally, TiO_2 xerogels were obtained after drying at 100 °C for 7 h and calcination at 500 °C for 2.5 h; the as-prepared TiO_2 xerogels were denoted as *x*% T80-TiO_2, where '*x*' is the used T80%.

2.3 Synthesis of TCPP-TiO_2 nanoparticles

TCPP was synthesized via a simple one-pot method in our previous work [38]. 0.1%TCPP-TiO_2 nanoparticles were synthesized via a simple wet impregnation method (Fig. 2b). Typically, 1 mg of TCPP was dissolved in 50 mL of methanol, then 1 g of TiO_2 powder was added to the solution which was magnetically stirred for 8 h. After 2 days of aging, TCPP-TiO_2

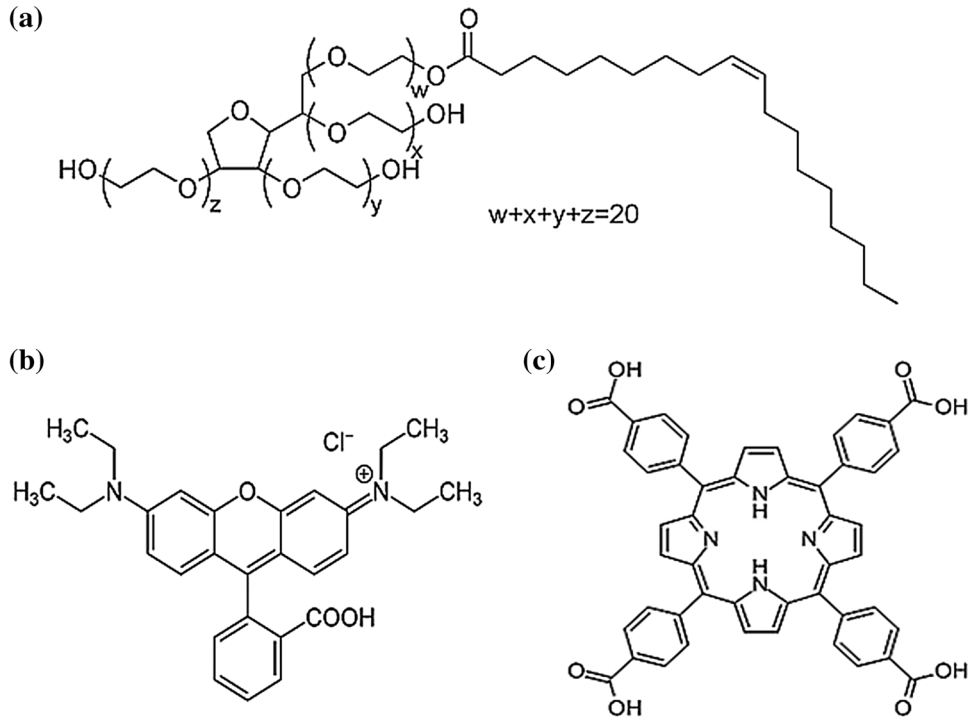

Fig. 1 Chemical structures of Tween 80 (**a**), Rhodamine B (**b**), and TCPP (**c**)

nanoparticles were subjected to filtration, washing several times by methanol, and finally dried at 100 °C for 2 h.

2.4 Physicochemical characterization

XRD patterns were recorded via X′PERT-PRO-PANalytical X-ray diffractometer (Netherlands) with CuKα radiation ($\lambda = 1.5406$ Å) in the 2θ range from 4° to 80° where the scanning mode was continuous, the step size was 0.02° and the scan step time was 0.5 s. The average crystallite sizes were estimated using Scherrer equation, Eq. 1:

$$D = \frac{k\lambda}{\beta \cos\theta} \tag{1}$$

where D is the average crystallite size (nm), k is the shape factor of the particles ($k = 0.9$), λ is the wavelength of the X-rays ($\lambda = 0.11540598$ nm), β and θ are the full width at half maximum of the peak (FWHM) and the diffraction angle (in radians), respectively.

The diffuse reflectance spectra (DRS) were recorded via Shimadzu UV-2600 UV–Vis spectrophotometer (Japan) over the range of 200–800 nm where Barium sulfate was utilized as reference material. The bandgap energy (E_g) of the as-prepared TiO_2 nanoparticles was calculated from the absorption edge by plotting the absorbance against energy (eV), Eq. 2:

$$E = h\nu = \frac{hc}{\lambda} = \frac{1240.8}{\lambda} \tag{2}$$

where h is Planck's constant (6.626×10^{-34} J s), E is the energy (eV), ν is the frequency, λ is the wavelength (nm), and c is the velocity of light (3×10^8 m/s).

Scanning electron microscopy (SEM) images were detected via JEOL, model Jed 2300 analysis station (Japan) to investigated the morphology of the solid surfaces at a working distance of 18–19 mm with an accelerating voltage of 20 kV. A high-resolution transmission electron microscope (HR-TEM, Tecnai G20, FEI, Netherlands) was utilized for imaging.

N_2 adsorption–desorption isotherms were recorded using Nova 3200 system (USA). The Brunauer–Emmett–Teller (BET) method was used for estimation of the surface areas (BET). The Barrett–Joyner–Halenda (BJH) model [42, 43] was utilized for the evaluation of the average pore size.

2.5 Reactor setup and photocatalytic measurements

The photocatalytic activities of x% T80-TiO_2 nanoparticles were estimated by following the degradation of RB dye under UV-A irradiation (15 W, Sylvania, Germany). A cylinder-shaped batch reactor (the diameter, R_d, is 10 cm) containing an exact weight of x%T80-TiO_2 and an exact volume of RB solution (10^{-5} M) was magnetically stirred at 400 rpm for 1 h in the dark to establish adsorption–desorption equilibrium. After that, the reactor was irradiated for 3 h with stirring at 400 rpm, where the vertical distance between the irradiation source and the reactor is fixed at 15 cm. 5 mL aliquots were withdrawn at definite time intervals during the

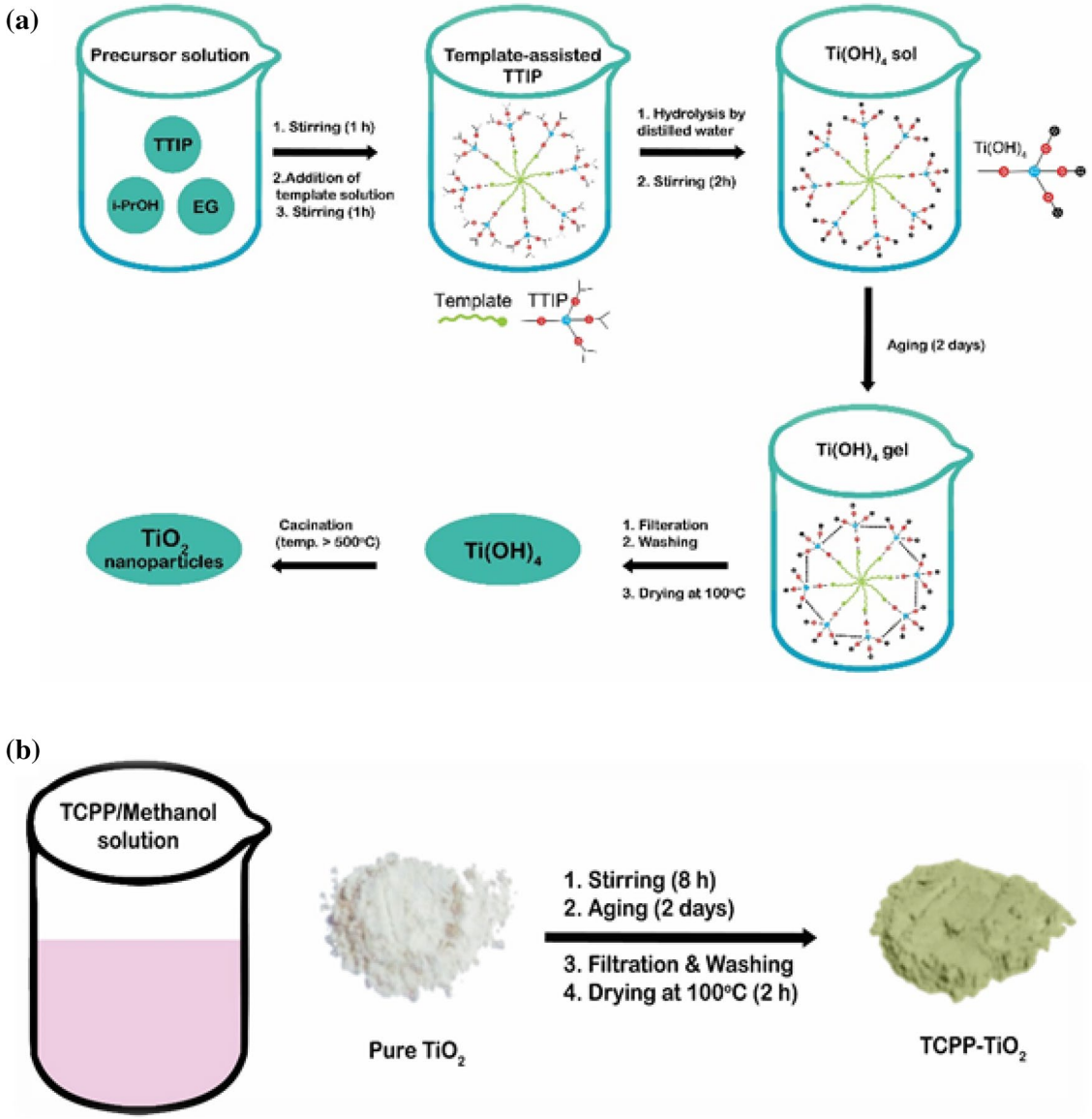

Fig. 2 Schematic diagram of the fabrication of x%T80-TiO_2 nanoparticles via the template-assisted sol–gel method (**a**), and TCPP-TiO_2 nanoparticles via wet impregnation method (**b**)

irradiation. Then, the photocatalyst powders were separated by centrifugation at 2000 rpm for 10 min, and the absorbance of the filtrates was recorded using a T92 + UV–Visible spectrophotometer (PG Instruments, UK) and the removal % of RB was estimated from Eq. 3:

$$\text{Removal } \% = \left[\left(A_o - A_t\right)/A_o\right] \times 100 \quad (3)$$

where A_o and A_t are the absorbance of RB after dark and at a time 't' of irradiation, respectively, at $\lambda_{max} = 554$ nm.

Visible light irradiation experiments were performed using a 90 W fluorescent lamp and 200 W Tungsten lamp, where a cylinder-shaped Pyrex vessel that surrounded by circulating water was used for cooling the system due to the high heat evolved from Tungsten lamp. HPLC spectra were recorded on a system that equipped with Waters 515 pump, sample injector, and Waters 2489 UV–Visible detector, which set at 554 nm for RB detection. HPLC separation of RB was executed via Waters C18 column (4.6 × 250 mm) in the reverse phase mode. The mobile phase was composed of equal volumes of acetonitrile and HPLC water (pH 4 was attuned by H_3PO_4) at a flow rate of 1 mL/min. The photodegradation % of RB was estimated from Eq. 4:

$$\text{Photodegradation } \% = \left[\left(PA_o - PA_t\right)/PA_o\right] \times 100 \quad (4)$$

where PA_o and PA_t are the peak area of RB after dark and after a time 't' of irradiation, respectively.

3 Results and discussion

3.1 Crystalline nature of x%T80-TiO_2 nanoparticles

XRD is an extensively used technique that involved in the investigation of the nature and size of crystalline phases of solid materials. The XRD patterns of all samples (Fig. 3a) had confirmed the presence of the Anatase phase based on the recorded peaks at $2\theta = 25.30$, 36.96, 37.76, 38.55, 48.05, 53.85, 55.10, 62.21, 62.65, 68.91, 70.36 and 75.08. All the samples have a single-crystalline phase, Anatase, except 5%T80-TiO_2 that contains mainly Anatase (Tetragonal) and very small percentages of Rutile (Tetragonal) and Brookite (Orthorhombic) crystalline phases. All the crystalline data, including the reference card numbers, space groups, and other cell parameters of the three crystalline phases, are stated in Table S1 in the supporting materials.

Obviously, T80% (5–50%) has a remarkable effect in the reduction of crystalline sizes (Fig. 3b) when compared to 0% T80-TiO_2 where 10%T80-TiO_2 had the smallest crystalline size as reported in Table 1. This approved the successful role of T80 template as a stabilizing agent in the preparation of TiO_2 via inhibition of particle growth to some extent during the hydrolysis and condensation process. These results

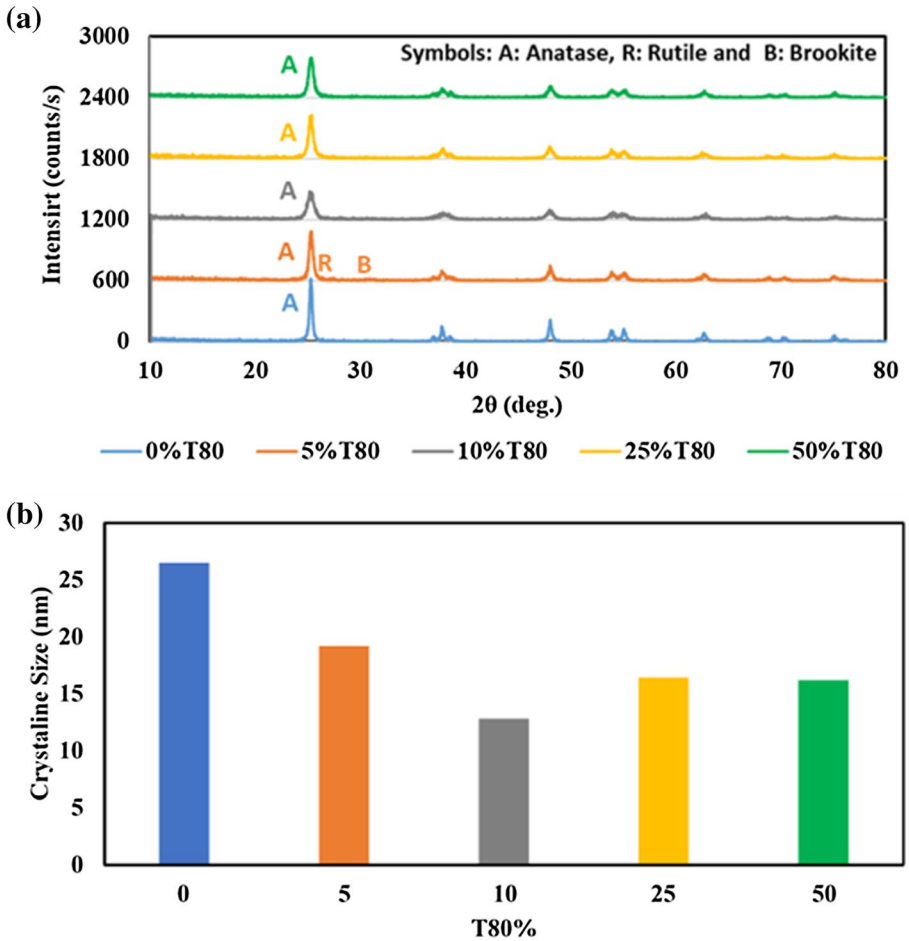

Fig. 3 Effect of T80% on the XRD patterns (**a**), and the crystalline sizes (**b**) of x%T80-TiO_2 nanoparticles

Table 1 Effect of T80% on the crystalline, optical and surface parameters of x%T80-TiO_2 nanoparticles

T80%	D (nm)	E_g (eV)	A_{BET} (m^2/g)	C-Const	V_p (cm^3/g)	$\bar{r}_p$ (Å)
0	26.5	3.1	10.95	17.14	0.0203	37.03
5	19.2	3.08	37.59	30.22	0.0699	37.18
10	12.8	3.12	54.20	62.67	0.0702	25.91
25	16.4	3.16	29.07	33.87	0.0484	33.32
50	16.2	3.17	21.70	16.36	0.0398	36.69

in good agreement with that reported earlier [44, 45] that utilized Tween 20 as a template in the synthesis of ZrO_2 and TiO_2 nanoparticles.

3.2 Texture properties and Surface parameters of *x*%T80-TiO_2 nanoparticles

The N_2 adsorption–desorption isotherms of 0–10%T80-TiO_2 nanoparticles are classified as type IV with a distinct plateau near saturation referred to limited adsorption of N_2 molecules (Fig. 4). The surface parameters such as specific surface area (A_{BET}), total pore volume (V_p) and average pore radius ($\bar{r}_p$) of *x*%T80-TiO_2 nanoparticles are mentioned in Table 1. The observed hysteresis loops in the desorption branches are categorized as type H2 according to the IUPAC classification. This type of hysteresis loop referred to an ink-bottle structure characterized by a narrow neck and wide bodies. It is remarkable to notice the increase in the size of the hysteresis loop in the sample prepared with 5%T80 and 10%T80 reflecting the positive role of T80 template in manipulating defined mesoporous structure.

The incorporation of high content of T80 leads to a deviation in its role in creating mesoporous structure as indicated by variation in the adsorption isotherm shape from type (IV) to type (II), which characterized by unlimited adsorption. One can argue that a process of pore shrinkage can occur to some extent in which pores approach closer and accumulate to each other, leading to converting the sample porosity from mesoporous to predominant macroporous structure. We can conclude that increasing T80% shifts the textural parameters to more negative direction reflecting that this high content prefers to segregate as separate micelles rather than its distribution between TiO_2 nanoparticles. Both the change in adsorption isotherm shape and the decrease in the surface area reflect the reduction in adsorption capacity, and this proportion becomes inaccessible to manipulate TiO_2 nanoparticles.

The pore size distribution curves (Fig. S1) reflects that the sample porosity is in the initial stage of mesoporosity (supermicropores) with a peak centered at nearly 20 Å. All the texture measurements have pointed out that the incorporation of low T80% (5–10%) during the progress of the preparation has a remarkable influence in improving the porosity of titania. The V_a–*t* plots (Fig. S2) are constructed to analyze the sample porosity. It is clearly observed that the V_a–*t* plot for the parent titania exhibits downward, and upward deviation reflects the existence of various numbers of micropores and mesopores. Incorporation of 5% and 10% of T80 did not affect the pore distribution. However, increasing in T80% up to 50% is accompanied by a reduction in the sample microporosity, which can be deduced from the disappearance of the downward deviation in the Va-t plot and remarkable decrease in surface area. This suggested the significant effect of T80% on the texture properties of the as-prepared TiO_2 nanoparticles and their corresponding surface parameters.

3.3 Optical properties of *x*%T80-TiO_2 nanoparticles

Diffuse reflectance spectra (DRS) were measured to show the absorption profiles of *x*%T80-TiO_2 catalysts (Fig. 5). The estimated and gap energies (Table 1) were found to be in the range of 3.1–3.2 eV, and this range is very near to the well-known reported value of pure Anatase TiO_2 (3.2 eV) [15, 17, 19, 20, 46–50] which is the predominant phase in all *x*%T80-TiO_2 catalysts. It is remarked that T80% (> 5%) has a minor influence on increasing the bandgap energy of TiO_2.

3.4 Morphology of *x*%T80-TiO_2 nanoparticles

SEM is a potent technique in the study of the morphology and the microstructure of nanoparticles. Obviously, there is a high percentage of homogeneity in the micromorphology of the groups of the nanoparticles that are found in a

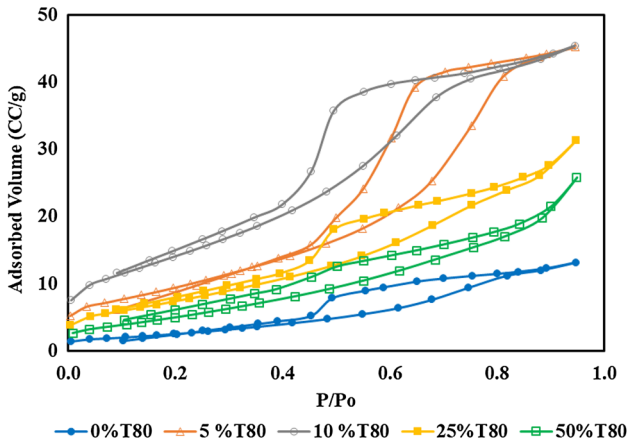

Fig. 4 N_2 adsorption–desorption isotherms of *x*%T80-TiO_2 catalysts

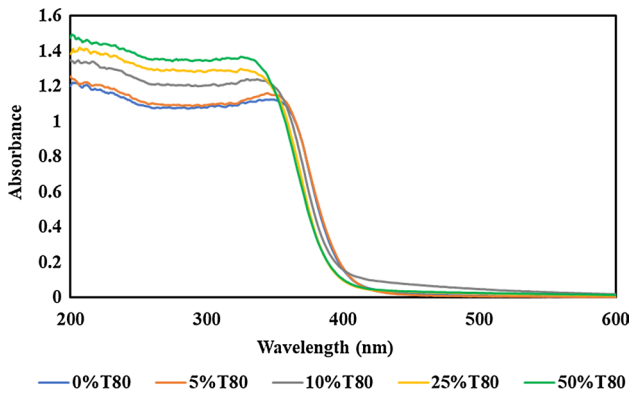

Fig. 5 The UV–Vis absorption spectra of *x*% T80-TiO_2 catalysts

microsphere order (Fig. 6a–c) in the range 0–10% of T80%. However, there is neither homogeneity nor a particular order of nanoparticles at higher T80% (25–50%), indicating that the high T80% severely affects the morphology of the nanoparticles (Fig. 6d, e).

HR-TEM is considered as a significant technique and obligatory for the investigation of nanomorphology of nanoparticles. Thus, it was used to study the effect of T80% on the nanostructure of TiO_2 nanoparticles (Fig. 7a–e). Clearly, the impact of T80% is apparent where non-uniform nanoparticles are obtained in the absence of T80 during the TiO_2 preparation (Figs. 7a, S3). While upon involving a low percent of T80, the obtained nanoparticles were found to be with uniform nanorods (5%T80-TiO_2, Figs. 7b, S4) and nanospheres (10%T80-TiO_2, Figs. 7c, S5). However, the higher T80% (25–50%) released non-uniform nanoparticles confirming that high T80% causes particle growth and severely affects the morphology and homogeneity of the nanoparticles obtained (Figs. 7d–e, S6-S7), as suggested from SEM images. Therefore, if someone aims to manipulate the T80 as a template in the synthesis of TiO_2 nanoparticles with tunable morphology, then it is highly recommended to utilize low T80% (5–10%) in the synthesis route.

3.5 Photoactivity of *x*%T80-TiO_2 catalysts

The photocatalytic activities of the synthesized *x*%T80-TiO_2 nanoparticles toward RB photodegradation were investigated and estimated via both UV–Visible spectrophotometry and HPLC techniques (Fig. 8). Obviously, 0%T80-TiO_2 nanoparticles have the lowest photocatalytic activity, and 5%T80-TiO_2 nanoparticles have the highest photocatalytic activity. That may be accredited to superior physicochemical properties of 5%T80-TiO_2 nanorods when compared with 0%T80-TiO_2 nanoparticles, such as the higher surface area and the smaller particles size. To some extent, this may clarify the critical role of T80 in the preparation of TiO_2 nanoparticles. Although 10%T80-TiO_2 nanoparticles have well-defined nanospheres besides having the largest surface area and the least average crystalline size, their photocatalytic activity is less than 5%T80-TiO_2 nanoparticles. This may be attributed to some extent to many reasons; the first may be the nanomorphology of TiO_2 nanoparticles that can be considered as the theatre on which the photodegradation process occurs, not only the surface area of the theatre is the solely vital factor of the success but also the whole quality of the players must also be attractive to audience. Thus, nanorods may be more efficient than nanospheres in this process; RB may adopt well with nanorod structure rather than with nanosphere. Besides, some of the very small 10%T80-TiO_2 nanoparticles may scatter the incident light to some extent causing decrease in the photodegradation activity. Finally, the existence of very small percent of the rutile phase in 5%T80-TiO_2 may be the secret behind their superior photocatalytic activity, as reported earlier [51, 52]. This significantly confirms the critical influence of T80% on the photocatalytic performance of the as-fabricated *x*%T80-TiO_2 nanoparticles.

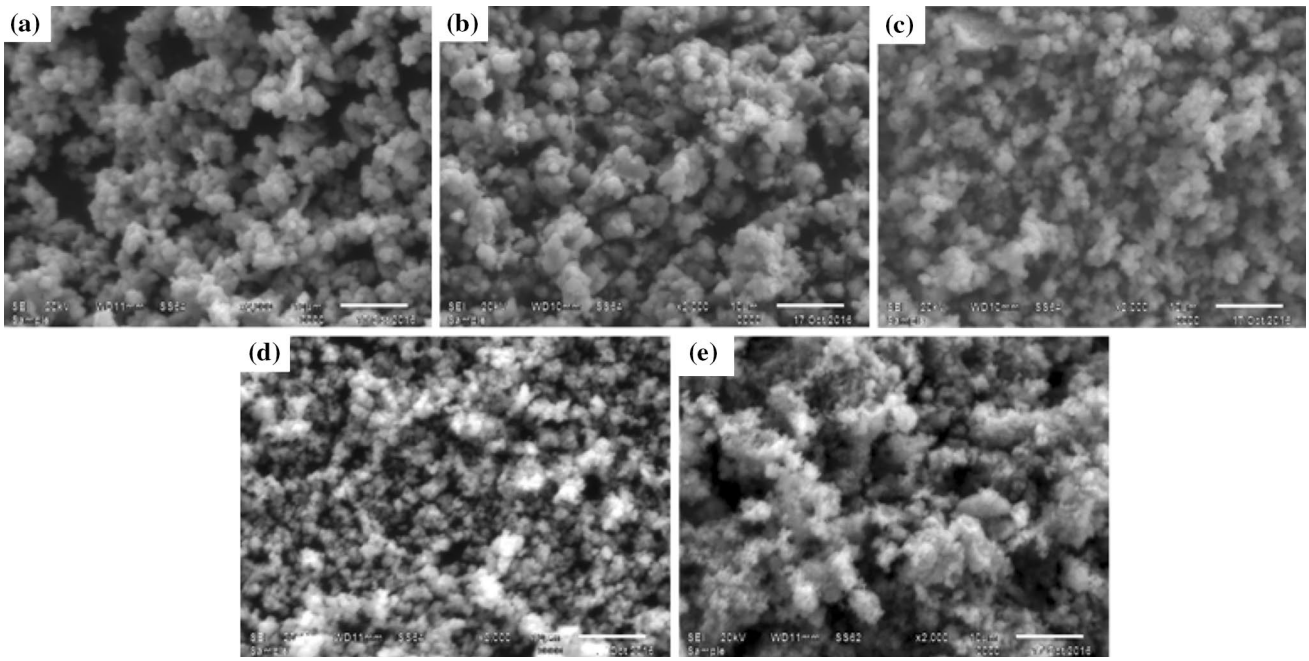

Fig. 6 SEM images of 0%T80-TiO_2 (**a**), 5%T80-TiO_2 (**b**), 10%T80-TiO_2 (**c**), 25%T80-TiO_2 (**d**) and 50%T80-TiO_2 (**e**) nanoparticles

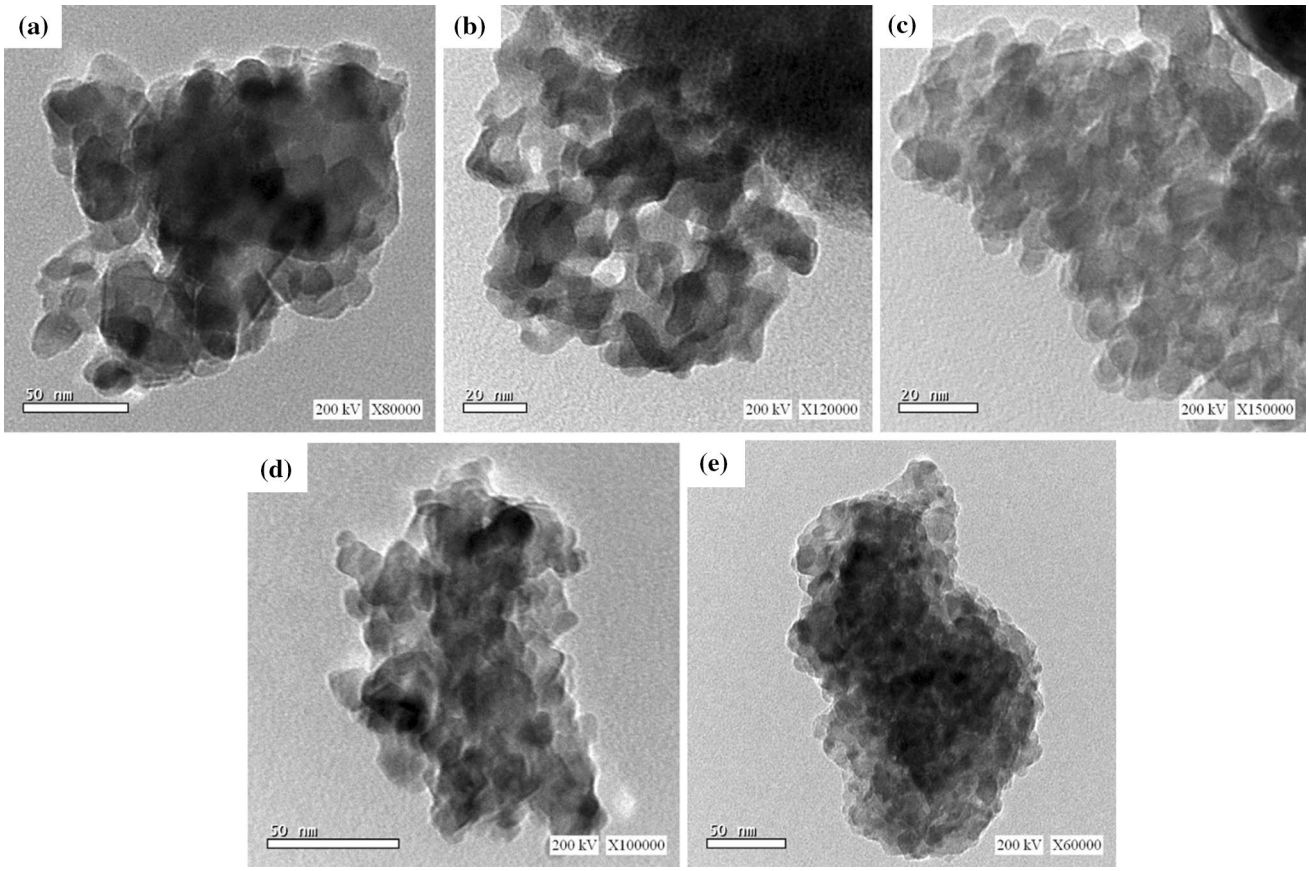

Fig. 7 HR-TEM images of 0%T80-TiO_2 (**a**), 5%T80-TiO_2 (**b**), 10%T80-TiO_2 (**c**), 25%T80-TiO_2 (**d**) and 50%T80-TiO_2 (**e**) nanoparticles

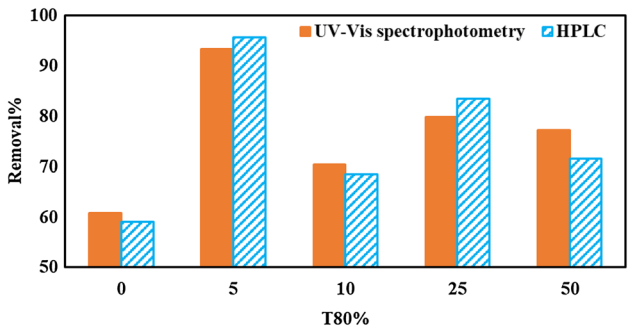

Fig. 8 The photocatalytic activities of x%T80-TiO_2 catalysts toward RB photodegradation under UV-A irradiation. ([Cat] = 1 g/L, $[RB]_o = 1 \times 10^{-5}$ M, pH 6, R_d = 10 cm, irradiation time = 180 min)

3.6 Enhancement of photocatalytic activity of T80-TiO_2 nanoparticles to visible light

In our previous work [38], TCPP was anchored on the surface of TiO_2 nanoparticles to act as a visible antenna to enhance its photocatalytic activity toward the visible light region. TCPP was found to have a brilliant role in improving the entire optical characteristics of TiO_2 by reducing the e–h recombination rate, reducing the bandgap energy and construction of a perfect visible antenna to recover its inefficiency in visible light region. Thus, 0.1%TCPP/5%T80-TiO_2 nanoparticles were synthesized to show the influence of TCPP on enhancement the photoactivity of and T80-TiO_2 nanorods under visible light.

The characteristic peaks of TCPP (S-band: 420 nm and Q-bands: 520, 550, 590 and 650 nm) were detected beside that of TiO_2 nanoparticles, Fig. 9, confirming the successful attaching of TCPP on TiO_2 surface [36, 53]. In addition, the bandgap energy reduced from 3.12 to 2.84 eV after anchoring TCPP on the surface of 5%T80-TiO_2 nanoparticles. Besides, the presence of other characteristic peaks of TCPP in the visible region is expected to act as a perfect visible antenna that enhances the photocatalytic performance of TiO_2 from the UV region to the visible region.

The photocatalytic activity of 0.1%TCPP/5%T80-TiO_2 nanoparticles was examined using various irradiation sources such as UV-A lamp, fluorescent lamp, and Tungsten lamp. Logically, the synthesized TCPP-TiO_2 nanoparticles exhibited an enhancement in the photocatalytic activity under both UV-A and visible irradiations, as shown from Table 2 and Fig. 10. It is interesting

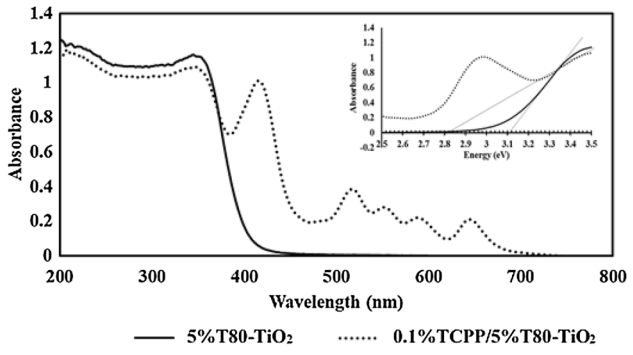

Fig. 9 Effect of TCPP on the absorption profile of 5%T80-TiO_2 nanoparticles (Inset: the corresponding Absorbance-Energy plot)

to notice that RB completely degraded using TCPP-TiO_2 after only 3 h of exposure to the irradiations of UV-A lamp or fluorescent lamp (Fig. 10a, b).

In our previous study [38], RB was completely degraded under UV-A and fluorescent lamp after 10 h of irradiation (Fig. 10d, e). This confirmed the improvement of the photocatalytic activity of TiO_2, which prepared through T80 template-assisted sol–gel method as well as its whole physical properties as previously explored. In addition, it is interesting to notice a remarkable blue shift in λ_{max} of RB that changed from 554 to 498 nm after 10 h of irradiation under Tungsten lamp using 0.1%TCPP/5%T80-TiO_2 nanoparticles (Fig. 10c). This shift may be due to the deethylation of amino groups of RB dye, as previously reported [54, 55]. This happened with 0.1%TCPP/template-free TiO_2 upon exposure to Tungsten lamp for 12 h while the removal percent was lower, so the observed shift was only from 554 to 542 nm (Fig. 10f). To recapitulate, having presented these results, it can be stated that TCPP successfully acted as a successful visible antenna for T80-TiO_2 nanoparticles which opens a wide range of enhanced applications of TiO_2 under direct solar irradiation. In addition, the T80-assisted sol–gel method improved the whole physical properties of TiO_2 when compared with the template-free sol–gel method.

3.7 Mechanism of action of Tween 80 as a template

The sol–gel method is utilized to synthesize TiO_2 nanoparticles, titanium alkoxide precursors are hydrolyzed then condensed to fabricate the Ti–O–Ti network. However, the sol–gel process may be accompanied by the formation of the amorphous particles with undefined morphologies with lower surface area and moderate performance [38, 56]. Therefore, the utilization of surfactant self-assemblies such as Tween 80 in a modified template-assisted sol–gel route is highly recommended to obtain homogeneous and highly ordered nanoparticles. Thus, the type and concentration of the employed template as a self-assembled template is a key factor to fabricate and tune the pore structure of inorganic materials. The mechanism of action of Tween 80 as a template could be described in the following steps. First, the TTIP precursor is dissolved in a large amount of isopropanol to ensure high dispersion of the precursor and avoid the agglomeration of particles as possible. Based on the amphoteric nature of surfactants, a certain percent of T80 is added to direct the molecules of Ti-precursor around it (Fig. 11). In the hydrolysis step, the added distilled water converted TTIP into $Ti(OH)_4$ sol that firmly attached to T80 micelles (rich in hydroxyl group Fig. 1a) via hydrogen bonds and Van der Waals attraction forces. During the aging period, condensation reactions of the formed precursors occur, leading to the construction of titania-based organic–inorganic hybrid copolymer networks [44]. Finally, the calcination at 500 °C is required to convert Titanium hydroxide into the crystalline phases of Titanium oxide and eliminate template micelles and other organic residuals such as isopropanol. To sum up, all the above-mentioned results of the physicochemical characterizations and the photocatalytic performance of the as-fabricated *x*%T80-TiO_2 nanoparticles confirmed the critical role of Tween 80 as an efficient and green template in the tuning of the properties of TiO_2 nanoparticles. In addition, it can be argued that not only did the incorporation of Tween T80 in the synthesis route affect the physical properties and photocatalytic activity of TiO_2 nanoparticles, but its percentage also affected them. Consequently, it is highly recommended that scholars could utilize this green template in the synthesis of various nanomaterials, it is expected that it may show unprecedented, enhanced, and unique properties.

Table 2 Effect of light sources on RB photodegradation using 0.1%TCPP/5%T80-TiO_2 and 0.1%TCPP/template-free TiO_2 ([Cat] = 1 g/L, $[RB]_o = 1 \times 10^{-5}$ M, $R_d = 10$ cm, pH 6)

Light source	UV-A lamp (15 W)	Fluorescent lamp (90 W)	Tungsten lamp (200 W)
0.1%TCPP/5%T80-TiO_2			
Removal %	97.41% (3 h)	95.36% (3 h)	88.93% (6 h)
k (min^{-1})	0.0202	0.0162	0.0083
0.1%TCPP/template-free TiO_2 [38]			
Removal %	93.46% (10 h)	93% (10 h)	28.23 (10 h)
k (min^{-1})	0.0051	0.0052	0.0006

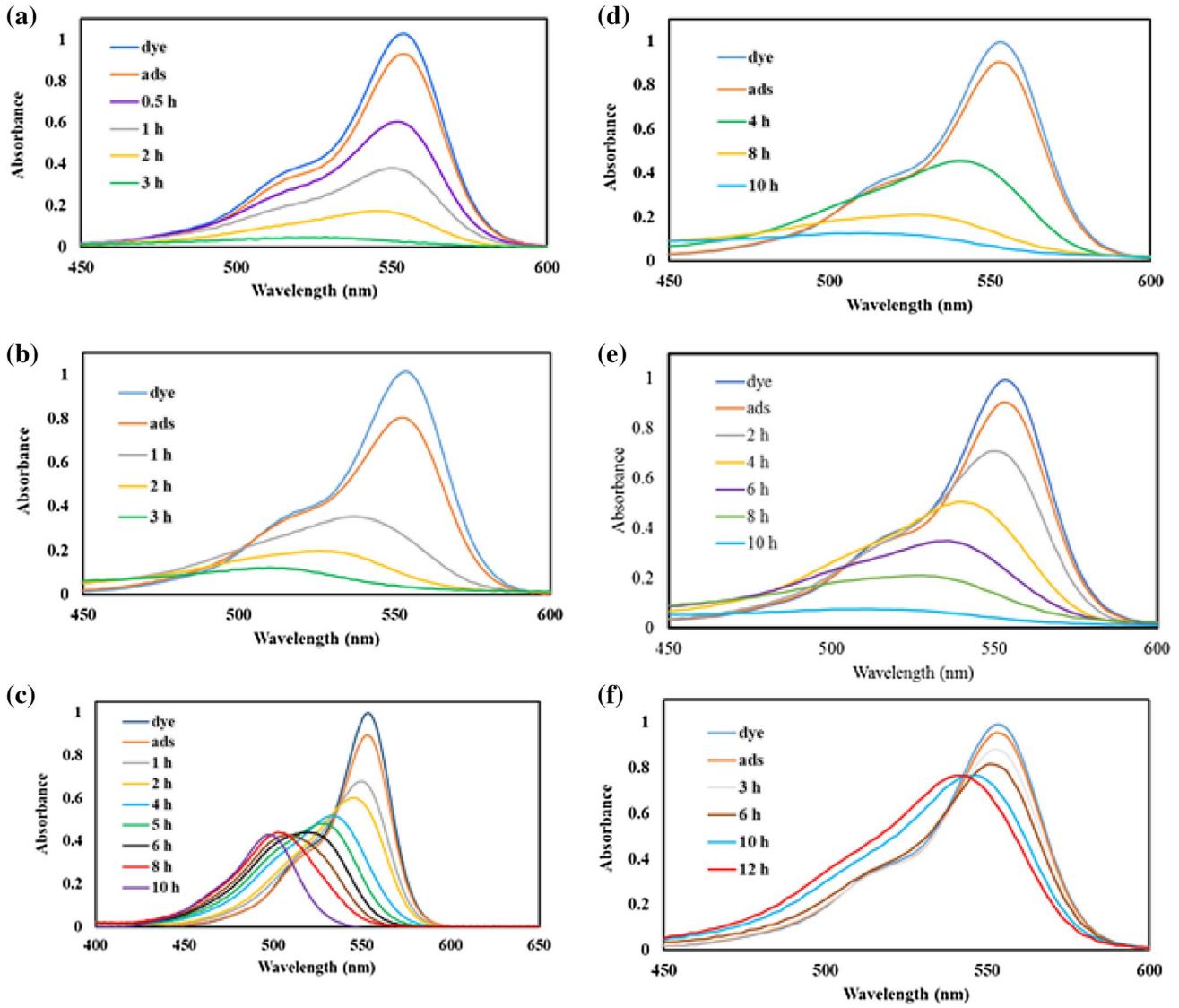

Fig. 10 Effect of different light sources such as UV-A lamp (**a**, **d**), visible fluorescent lamp (**b**, **e**) and Tungsten lamp (**c**, **f**) on the photodegradation of RB using 0.1%TCPP/5%T80-TiO_2 (**a**–**c**) and 0.1%TCPP/template-free TiO_2 (**d**–**f**), respectively. ([Cat] = 1 g/L, $[RB]_o = 1 \times 10^{-5}$ M, pH 6, $R_d = 10$ cm)

4 Conclusion

In conclusion, we have fabricated a series of TiO_2 nanoparticles with the utilization of different concentrations of Tween 80 as a pore-directing agent. It was found that T80% basically affected the quality, homogeneity, and morphology of the obtained nanoparticles and consequently affected their photocatalytic activity. The assembly of the mesoporous structure of TiO_2 nanoparticles is mainly due to the existence of hydrogen bonding between Tween 80 and $Ti(OH)_4$. Nanorods were the most reactive species toward RB photodegradation under UV-A. TCPP performed as a perfect visible antenna for T80-TiO_2 nanoparticles, which enhance the range of application of TiO_2 under direct solar irradiation. These novel nanoparticles are expected to be promising candidates not only for photodegradation of different organic pollutants but also for other promising applications. Finally, T80 is expected to show promising properties if it is manipulated in the fabrication of various nanoparticles.

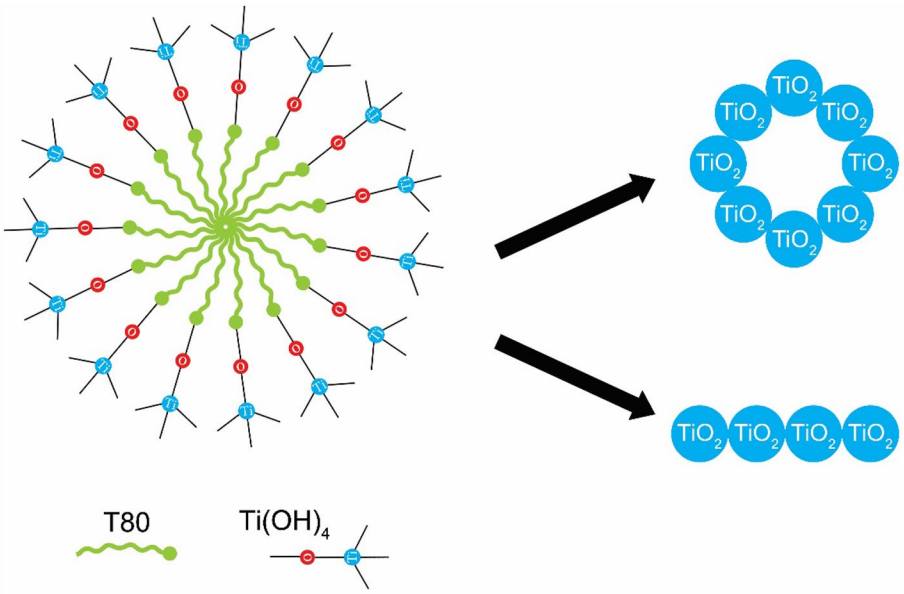

Fig. 11 Schematic diagram of the titania-based organic–inorganic hybrid network [Tween 80-$Ti(OH)_4$] into TiO_2 nanoparticles through calcination at 500 °C

Funding This research did not receive any specific Grant from funding agencies in the public, commercial, or not-for-profit sectors.

References

1. I.K. Konstantinou, T.A. Albanis, Appl. Catal. B **49**, 1 (2004)
2. N.M. Mahmoodi, M. Arami, N.Y. Limaee, N.S. Tabrizi, Chem. Eng. J. **112**, 191 (2005)
3. M.Y. Rezk, M. Zeitoun, A.N. El-Shazly, M.M. Omar, N.K. Allam, J. Hazard. Mater. **378**, 120679 (2019)
4. M.A. Hamza, A.N. El-Shazly, S.A. Tolba, N.K. Allam, Chem. Eng. J. **384**, 123351 (2020)
5. D. Xu, S. Cao, J. Zhang, B. Cheng, J. Yu, Beilstein J. Nanotechnol. **5**, 658 (2014)
6. M.A. Ahmed, Z.M. Abou-Gamra, A.M. Salem, J. Environ. Chem. Eng. **5**, 4251 (2017)
7. A. Beitollahi, A. Hossein, H. Daie, L. Samie, M. Mehdi, J. Alloys Compds. **490**, 311 (2010)
8. H. Choi, E. Stathatos, D.D. Dionysiou, Appl. Catal. B **63**, 60 (2006)
9. W. Li, M. Zhang, J. Zhang, Y. Han, Front. Chem. China **1**, 438 (2006)
10. V. Bhatia, A. Dhir, J. Environ. Chem. Eng. **4**, 1267 (2016)
11. N. Chaukura, S.S. Mukonza, T.I. Nkambule, B.B. Mamba, Int. J. Environ. Sci. Technol. **16**, 1603–1612 (2018)
12. M.A. Hamza, A.N. El-Shazly, N.K. Allam, Mater. Lett. **262**, 127188 (2020)
13. M. Nasirian, Y.P. Lin, C.F. Bustillo-Lecompte, M. Mehrvar, Int. J. Environ. Sci. Technol. **15**, 2009 (2018)
14. A. Jraba, Z. Anna, E. Elaloui, Sci. Mater. Electron. **22**, 648–658 (2019)
15. V. Vaiano, O. Sacco, D. Sannino, P. Ciambelli, Chem. Eng. J. **261**, 3 (2015)
16. S.M. El-Sheikh, G. Zhang, H.M. El-Hosainy, A.A. Ismail, K.E. O'Shea, P. Falaras, A.G. Kontos, D.D. Dionysiou, J. Hazard. Mater. **280**, 723 (2014)
17. W. Yu, X. Liu, L. Pan, J. Li, J. Liu, J. Zhang, P. Li, C. Chen, Z. Sun, Appl. Surf. Sci. **319**, 107 (2014)
18. J. Geng, D. Yang, J. Zhu, D. Chen, Z. Jiang, Mater. Res. Bull. **44**, 146 (2009)
19. A. Siddiqa, D. Masih, D. Anjum, M. Siddiq, J. Environ. Sci. **37**, 100 (2015)
20. X. Chen, X. Zhang, Y. Su, L. Lei, Appl. Surf. Sci. **254**, 6693 (2008)
21. D.R. Zhang, H.L. Liu, S.Y. Han, W.X. Piao, J. Ind. Eng. Chem. **19**, 1838 (2013)
22. M. Wei, N. Song, F. Li, Z.N. Qi, M.M. Yao, J. Mater. Sci. Mater. Electron. **28**, 6320 (2017)
23. Z. Guo, B. Chen, J. Mu, M. Zhang, P. Zhang, Z. Zhang, J. Wang, X. Zhang, Y. Sun, C. Shao, Y. Liu, J. Hazard. Mater. **219–220**, 156 (2012)
24. Z.M. Abou-Gamra, M.A. Ahmed, J. Photochem. Photobiol. B **160**, 134 (2016)
25. H. Wang, D. Zhou, Z. Wu, J. Wan, X. Zheng, L. Yu, D.L. Phillips, Mater. Res. Bull. **57**, 311 (2014)
26. C. Wang, J. Li, G. Mele, M.Y. Duan, X.F. Lü, L. Palmisano, G. Vasapollo, F.X. Zhang, Dye. Pigment. **84**, 183 (2010)
27. J. Niu, B. Yao, Y. Chen, C. Peng, X. Yu, J. Zhang, G. Bai, Appl. Surf. Sci. **271**, 39 (2013)
28. S. Murphy, C. Saurel, A. Morrissey, J. Tobin, M. Oelgemöller, K. Nolan, Appl. Catal. B **119–120**, 156 (2012)
29. A. Kathiravan, V. Anbazhagan, M. Asha Jhonsi, R. Renganathan, Spectrochim. Acta Part A **70**, 615 (2008)
30. A. Kathiravan, R. Renganathan, J. Colloid Interface Sci. **331**, 401 (2009)
31. G. Granados-Oliveros, E.A. Páez-Mozo, F.M. Ortega, M. Piccinato, F.N. Silva, C.L.B. Guedes, E. Di Mauro, M.F. da Costa, A.T. Ota, J. Mol. Catal. A **339**, 79 (2011)
32. M.Y. Duan, J. Li, M. Li, Z.Q. Zhang, C. Wang, Appl. Surf. Sci. **258**, 5499 (2012)
33. J.-H. Cai, J.-W. Huang, H.-C. Yu, L.-N. Ji, Int. J. Photoenergy **2012**, 1 (2012)

34. E. Gholamrezapor, A. Eslami, J. Mater. Sci. Mater. Electron. **30**, 4705 (2019)
35. H. Huang, X. Gu, J. Zhou, K. Ji, H. Liu, Y. Feng, Catal. Commun. **11**, 58 (2009)
36. C. Huang, Y. Lv, Q. Zhou, S. Kang, X. Li, J. Mu, Ceram. Int. **40**, 7093 (2014)
37. M.Y. Chang, Y.H. Hsieh, T.C. Cheng, K.S. Yao, M.C. Wei, C.Y. Chang, Thin Solid Films **517**, 3888 (2009)
38. M.A. Ahmed, Z.M. Abou-Gamra, H.A.A. Medien, M.A. Hamza, J. Photochem. Photobiol. B **176**, 25 (2017)
39. Y. Khan, S.K. Durrani, M. Siddique, M. Mehmood, Mater. Lett. **65**, 2224 (2011)
40. M. Kazemi, M.R. Mohammadizadeh, Chem. Eng. Res. Des. **90**, 1473 (2012)
41. C. Han, J. Andersen, V. Likodimos, P. Falaras, J. Linkugel, D.D. Dionysiou, Catal. Today **224**, 132 (2014)
42. E.P. Barrett, L.G. Joyner, P.P. Halenda, J. Am. Chem. Soc. **73**, 373 (1951)
43. L.G. Joyner, E.P. Barrett, R. Skold, J. Am. Chem. Soc. **7**, 3155 (1951)
44. Y. Chen, S.K. Lunsford, Y. Song, H. Ju, P. Falaras, V. Likodimos, A.G. Kontos, D.D. Dionysiou, Chem. Eng. J. **170**, 518 (2011)
45. Y. Chen, E. Stathatos, D.D. Dionysiou, Surf. Coat. Technol. **202**, 1944 (2008)
46. H. Feng, M.-H. Zhang, L.E. Yu, Appl. Catal. A **413–414**, 238 (2012)
47. X.F. Lü, W.J. Sun, J. Li, W.X. Xu, F.X. Zhang, Spectrochim. Acta Part A **111**, 161 (2013)
48. E.P. Melián, O.G. Díaz, J.D. Rodríguez, G. Colón, J.A. Navío, J.P. Peña, Appl. Catal. A **153**, 411–412 (2012)
49. W. Vallejo, C. Diaz-Uribe, Á. Cantillo, J. Photochem. Photobiol. A **299**, 80 (2015)
50. C. Belver, J. Bedia, M.A. Álvarez-Montero, J.J. Rodriguez, Catal. Today **266**, 36 (2016)
51. S. Bakardjieva, J. Šubrt, V. Štengl, M.J. Dianez, M.J. Sayagues, Appl. Catal. B **58**, 193 (2005)
52. J. Choi, H. Park, M.R. Hoffmann, J. Phys. Chem. C **114**, 783–792 (2016)
53. L. Tasseroul, S.D. Lambert, D. Eskenazi, M. Amoura, C.A. Páez, S. Hiligsmann, P. Thonart, B. Heinrichs, J. Photochem. Photobiol. A **272**, 90 (2013)
54. Z.M. Abou-Gamra, M.A. Ahmed, M.A. Hamza, Nanotechnol. Environ. Eng. **2**, 12 (2017)
55. Q. Wang, J. Li, Y. Bai, X. Lu, Y. Ding, S. Yin, H. Huang, H. Ma, F. Wang, B. Su, J. Photochem. Photobiol. B **126**, 47 (2013)
56. A.M. Fadl, M.I. Abdou, S.A. Al-Elaa, M.A. Hamza, S.A. Sadeek, Prog. Org. Coat. **136**, 105263 (2019)